

# LEMON-Mapping: Loop-Enhanced Large-Scale Multi-Session Point Cloud Merging and Optimization for Globally Consistent Mapping

Lijie Wang<sup>1</sup>, Xiaoyi Zhong<sup>1</sup>, Ziyi Xu<sup>1</sup>, Kaixin Chai<sup>2</sup>, Anke Zhao<sup>1</sup>, Tianyu Zhao<sup>1</sup>, Qianhao Wang<sup>1,†</sup>, Fei Gao<sup>1,†</sup>

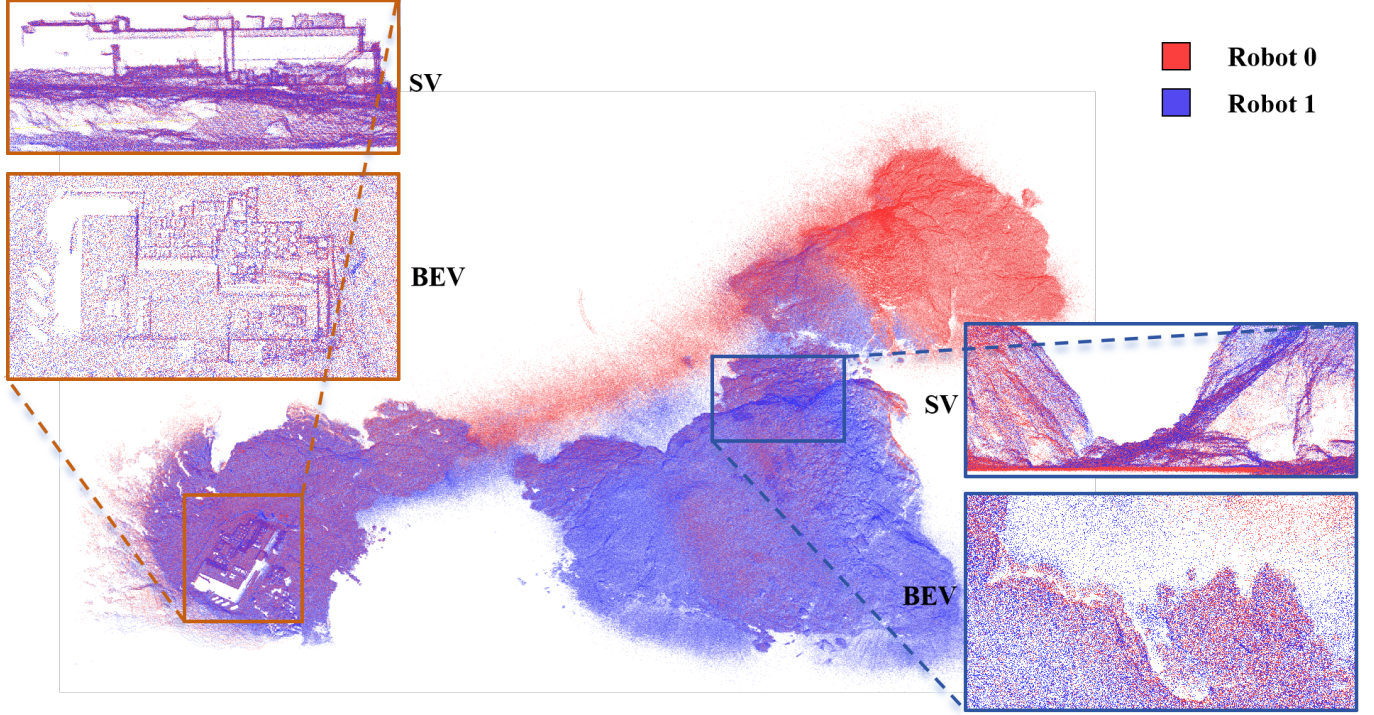


Fig. 1: The merging map of our framework in island sequence of MARS-LVIG [1] dataset, the details in the figure are framed and shown in two forms: side view (SV) and bird's eye view (BEV).

**Abstract**—With the rapid development of robotics, multi-robot collaboration has become critical and challenging. One key problem is integrating data from multiple robots to build a globally consistent and accurate map for robust cooperation and precise localization. While traditional multi-robot pose graph optimization (PGO) maintains basic global consistency, it focuses primarily on pose optimization and ignores the geometric structure of the map. Moreover, PGO only uses loop closure as a constraint between two nodes, failing to fully exploit its capability to maintaining local consistency of multi-robot maps. Therefore, PGO-based multi-robot mapping methods often suffer from serious map divergence and blur, especially in regions with overlapping submaps. To address this issue, we propose Lemon-Mapping, a loop-enhanced framework for large-scale multi-session point cloud map fusion and optimization, which reasonably utilizes loop closure and improves the geometric quality of the map. We re-examine the role of loops for multi-robot mapping and introduce three key innovations. First, we develop a robust loop processing mechanism that effectively rejects outliers and a novel loop recall strategy to recover mistakenly removed loops. Second, we introduce a spatial bundle adjustment method for multi-robot maps that significantly reduces the divergence in overlapping regions and eliminates map blur. Third, we design a PGO strategy that leverages the refined constraints of bundle adjustment to extend the local accuracy to the global map.

We validate our framework on several public datasets and a self-collected dataset. Experimental results demonstrate that our method outperforms traditional map merging approaches in terms of mapping accuracy and reduction of map divergence. Scalability experiments also demonstrate the strong capability of our framework to handle scenarios involving numerous robots.

**Index Terms**—Multi-robot mapping, map merging, SLAM.

## I. INTRODUCTION

Large-scale 3D mapping is a fundamental capability in modern robotics, providing rich geometric information that supports tasks such as drone-based inspection [2]–[4], autonomous driving [5], and long-term exploration with ground robots [6]. Furthermore, large-scale 3D maps are also critical for emerging fields such as embodied AI, where agents interact with complex environments based on spatial understanding [7], and end-to-end visuomotor navigation systems [8], which rely on accurate environmental priors to improve generalization ability and robustness. Especially, multi-robot 3D mapping is essential for large-scale and complex tasks, where heterogeneous robot teams provide greater coverage and robustness compared to a single agent. In scenarios such as search and rescue [9], forest monitoring [10], and subterranean exploration [11], accurate point cloud fusion is vital to build

This paper was produced by the IEEE Publication Technology Group. They are in Piscataway, NJ.

Manuscript received April 19, 2021; revised August 16, 2021.

consistent and high-quality maps under complex and GPS-denied conditions.

Rapid development of LiDAR-based Simultaneous Localization and Mapping (SLAM) techniques [12]–[17] has enabled individual robots to perform real-time localization and point cloud map construction. However, one major challenge remains. Most existing lightweight SLAM systems [14]–[16] designed for onboard robot computers are based on direct LiDAR-Inertial-Odometry methods. These methods prioritize pose estimation over map construction to achieve real-time performance. However, the lack of feature extraction and matching in these approaches results in maps with blurred details and poor geometric accuracy. Therefore, the quality of the point cloud maps generated by onboard computers based on lightweight methods requires further improvement.

To address mapping challenges and enhance the geometric accuracy of point cloud maps, various optimization strategies have been proposed. Among them, one category of approaches leverages pose graph optimization (PGO) [18] to handle loop scenarios. Loop closure constraints detected by loop detection methods [19]–[22] are added to the pose graph [18] along with odometry constraints to eliminate accumulated drift and improve the global consistency of the map. However, PGO-based methods only use the point cloud map to extract descriptors during loop detection and ignore the structure and geometric information. Therefore, the problem of inaccurate geometric structure and blurred map is not fundamentally solved. (We provide examples in Fig. 9 (b) and (c)). In contrast, another type of map refinement method based on bundle adjustment (BA) has demonstrated impressive capabilities to enhance point cloud maps in recent years [23]–[26]. These approaches utilize the structural characteristics of the point cloud map and improve its quality by minimizing the geometric residuals between feature points and feature structure. Nevertheless, the temporal-sequential nature of these methods limits their ability to actively and effectively leverage loop closure information when dealing with scenarios involving multiple revisits to the same area, which may ultimately lead to degraded global consistency (as illustrated in Fig. 8 (b) and (c)). The dependence on the chronological ordering of poses also limits the applicability of BA-based methods to multi-robot systems.

In addition to the above mapping approaches, to achieve larger-scale map reconstruction and multi-robot collaboration, several multi-robot SLAM systems [27], [28] and offline map fusion techniques [29]–[33] have shown promising results in recent years. In general, these methods focus on two aspects: removing outliers in loop closure data and achieving map fusion through multi-robot pose graph optimization. However, as discussed in the previous paragraph, PGO-based methods neither directly utilize the geometric information of multi-robot maps nor fully leverage loop closure data. Therefore, these methods only roughly ensure the basic alignment and consistency of the global map, but they fall short in producing high-quality point cloud maps. In particular, they often suffer from blur and misalignment in regions with overlap between robots (as demonstrated in the comparison results in Fig. 9 (b) and (c)).

Inspired by the strengths and limitations of the aforemen-

tioned approaches, we conduct an in-depth analysis of previous multi-robot SLAM systems and map merging systems. We argue that the merging of point cloud maps is essentially a **map-driven local point cloud registration problem** rather than a pose-dominated pose optimization problem. Building upon this perspective, we identify two essential challenges for achieving effective multi-robot point cloud map fusion: **(1)** Map fusion should be treated as a map-driven registration problem rather than a pose-centric optimization task, and PGO alone can not solve this problem. **(2)** Loop closure information should be fully exploited in registration beyond time-sequential constraints to ensure both global consistency and local accuracy.

To overcome the above challenge, we propose **LEMON-Mapping**, a **Loop-Enhanced large-scale Multi-session map merging and Optimization** framework that achieves globally consistent and geometrically accurate point cloud mapping. Our framework re-examines the ability of loop closure and reasonably enhances its role by two aspects, which effectively improves the consistency of merged map and eliminates the divergence in overlapping area (shown in Fig. 9). First, we innovatively recall loops that are mistakenly removed after obtaining the prior information of multi-robot trajectories, providing more sufficient information and optimization starting points for subsequent spatial bundle adjustment. Second, by leveraging sufficient valid loop closures, our proposed spatial bundle adjustment overcomes the limitation of traditional bundle adjustment methods that operate only on single-robot maps. The spatial bundle adjustment is performed within a local spatial window around the loop, effectively leveraging multiple observations and abundant constraints from different robots. It directly optimizes the poses from different robots equally within the window; thus, the poses of multiple robots matching the same geometric features (planes, lines) are adjusted simultaneously, generating a locally accurate and consistent map. Although spatial bundle adjustment improves local map accuracy at loop closures, it lacks the capability for global map fusion. To address this problem, we propose a reasonable PGO-based way to transfer the local alignment achieved by our spatial BA to the whole map, which effectively combines local BA constraints and odometry constraints to attain a globally consistent and accurate map. We conduct a series of extensive experiments, and the results demonstrate the high mapping accuracy and strong scalability of our multi-session map fusion approach, as shown in Fig. 1 and Fig. 14.

In general, the main contributions of this work can be summarized as follows:

- A scalable multi-session point cloud map merging and optimization framework is designed, which integrates two-stage pose graph optimization with spatial bundle adjustment. The method achieves high-precision 3D mapping reconstruction in large-scale and multi-robot scenarios.
- A novel spatial bundle adjustment that can be used for multi-robot mapping is introduced, which operates on loop-based spatial windows to fully utilize loop constraints and jointly optimize multi-robot poses equally. This improves the local accuracy and eliminates the

serious map divergence.

- A pose graph optimization scheme with reasonable sparsification of BA constraints is developed, which effectively propagate local accuracy to the global scale, improving both consistency and efficiency.
- A robust loop closure processing pipeline is designed, including outlier rejection and false negative recall, which enhances the reliability and completeness of loop constraints used for map fusion.

## II. RELATED WORKS

### A. Single Map Maintenance and Optimization

Single map maintenance and optimization have been extensively studied, with existing approaches falling broadly into two categories: pose graph optimization (PGO) and bundle adjustment (BA) based methods. PGO remains a widely adopted back-end in LiDAR SLAM systems [34]–[36]. A single-robot pose graph is constructed to refine initial pose estimates from odometry by utilizing the constraints of loop closure. However, traditional PGO frameworks focus on pose consistency rather than directly optimizing point cloud structure, leading to map with poor geometric quality, which limits their effectiveness in generating globally consistent maps for precision-demanding applications.

In contrast, BA-based methods jointly optimize scan poses and scene features by minimizing the geometric residuals of matched primitives, offering improved map accuracy. BALM [23] introduces a closed-form solution for feature parameters to reduce computational complexity, while BALM2 [24] extends this with point clustering and a more efficient second-order solver. HBA [25] adopts a hierarchical BA strategy followed by top-down PGO, significantly improving the quality and consistency of the overall map. PSS-BA [26] introduces quadratic surface modeling for point cloud maps and uses progressive smoothing iteration to optimize map quality. RSO-BA [37] improves robustness via a second-order estimator integrated with a robust kernel function. However, traditional bundle adjustment approaches rely on time-based sliding windows and fail to incorporate long-range spatial constraints introduced by loop closures. These constraints of loop closures, though temporally distant, are spatially adjacent with sharing of the same geometric features and crucial for improving local consistency. To address this gap, we propose a novel BA formulation based on local spatial windows that better leverages spatial correlations for more accurate and consistent mapping.

### B. Multi-Session Map Merging

Multi-session map merging aims to integrate submaps from multiple agents either with or without initial pose estimates into a unified, globally consistent map. SegMap [38] extracts semantic features from 3D point clouds to estimate 6-DoF transformations and utilizes incremental pose graph optimization to achieve map fusion. However, it heavily depends on accurate semantic segmentation, limiting its applicability to structured urban environments. AutoMerge [30] introduces a city-scale merging framework that avoids relying on initial

alignment, but its performance degrades in complex environments due to the lack of elimination of loop outliers. PCM [31]–[33] selects reliable loop sequences through pairwise consistency maximization, but struggles on datasets with high loop error rates. It is also severely affected by the accumulated drift of odometry in large-scale environments. LAMM [29] enhances place recognition by removing dynamic objects through M-Detector [39] and using the robust loop detection method BTC [20], yet it only merges map by pose graph optimization, which may suffer from local divergence in the overlapping areas of the multi-robot map.

Outlier rejection constitutes another critical concern in multi-session map merging system. This is because large-scale environments often contain repetitive structures, increasing the risk of incorrect data association and false positive loop closures. Thus, the robust rejection of outliers is essential. RANSAC [40] remains a standard solution by fitting models despite outliers, but its effectiveness diminishes under high outlier ratios and in cases lacking strong priors. PCM [31], adopted in systems such as DCL-SLAM [27] and Disco-SLAM [28], leverages pairwise geometric consistency for loop validation. Although PCM is more robust under uncertain initial estimates, its accuracy can be compromised by unreliable odometry, resulting in over-rejection of valid loop closures.

## III. METHODOLOGY

### A. System Overview

#### Problem Formulation.

Our objective is to construct an accurate and globally consistent map by merging multiple submaps generated from different robots. In LiDAR-based SLAM systems [12]–[14], [16], each scanned point cloud is considered rigidly connected to the LiDAR, and the global point cloud map is constructed by transforming each scan into the world coordinate system utilizing its corresponding pose. Therefore, the quality of the point cloud map is strictly associated with the sensor pose at the time of acquisition.

In a multi-robot system, the set of pose sequences can be denoted as  $S_N = \{s_1, s_2, \dots, s_N\}$ , where each sequence  $s_k$  corresponds to a separate robot. Different sequences (e.g.  $s_i$  and  $s_j$ ), which have different starting points and initial orientations, lack prior information about relative pose transformation. To achieve accurate and effective map fusion, it is essential to estimate the relative transformations between these trajectories and optimize the poses using constraints in overlapping regions to improve geometric consistency.

The problem can therefore be formulated as finding a set of optimized pose sequences  $S_N^* = \{s_1^*, s_2^*, \dots, s_N^*\}$ , in which all trajectories are aligned to a common coordinate system (typically  $s_1^*$ ), and the resulting global map exhibits minimal divergence in overlapping regions while maintaining overall consistency.

#### Framework of Lemon-Mapping.

An overview of the proposed framework is illustrated in Fig. 2, which consists of two main components: the Loop Processing Module (Fig. 2 (a)) detailed in Section III-B and the Map Merging Module (Fig. 2 (b)) described in Section III-C and III-D.

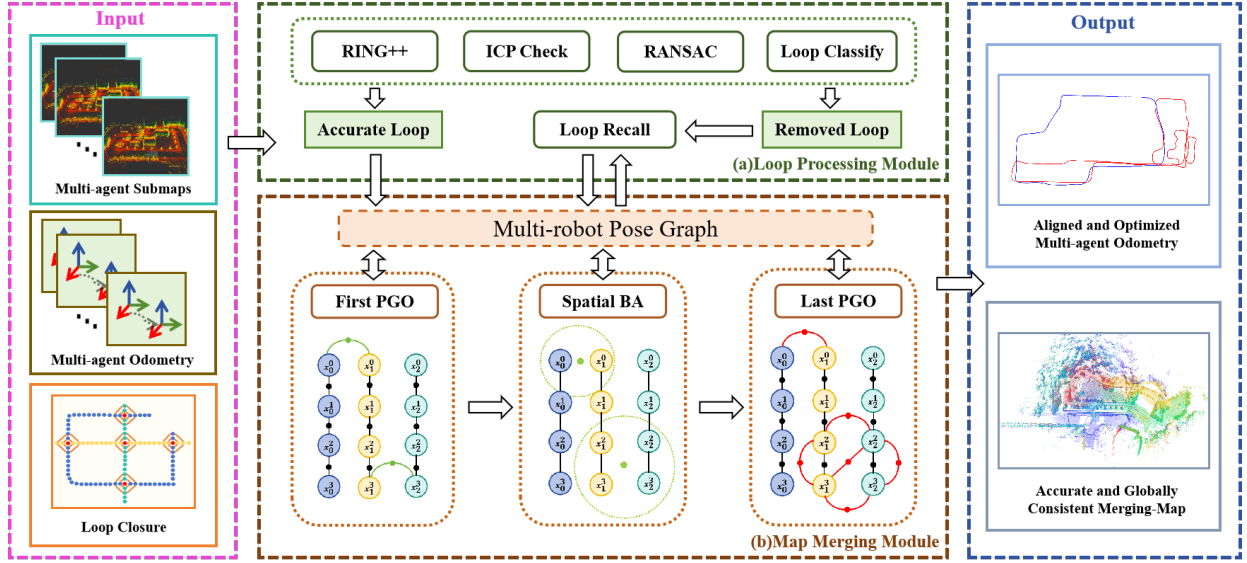


Fig. 2: The framework of our method. (a) The loop processing module. (b) The map Merging module. Our framework takes multi-agent submaps and odometry as input, and generates accurate and globally consistent merging map.

The Loop Processing Module takes the odometry and submaps from multiple agents as input, along with raw loop closure data (including both self-loops and inter-loops) and removes erroneous loops to output the correct loops. The Map Merging Module then uses the correct loops to optimize the multi-robot trajectories through three steps: spatial bundle adjustment and two pose graph optimization (PGO) steps. First, a preliminary global pose estimate is obtained using a conventional loop-based multi-robot pose graph optimization (the first PGO step), which serves as an initial guess and prior information for loop recall. Next, a spatial bundle adjustment is performed within local regions around the loops to fully exploit the geometric constraints from overlapping observations. Finally, the last PGO step refines the trajectories using bundle adjustment constraints and odometry constraints. As the two PGO steps share a similar formulation, they are jointly described in Section III-D, while the spatial bundle adjustment is discussed separately in Section III-C.

### B. Loop Processing Module

The loop processing module is a fundamental component that supports the spatial bundle adjustment described in Section III-C and the final map merging process in Section III-D. It consists of three submodules: Outlier Rejection, Loop Classification, and Loop Recall. This module processes both self-loops and inter-loops, which are initially detected by the robust and SOTA loop detection method RING++ [21].

#### Outlier Rejection.

Loop closure data, including self-loops and inter-loops, may contain incorrect entries, which significantly influences the accuracy of coordinate alignment and pose graph optimization. To solve this problem, we design an outlier rejection method using Generalized Iterative Closest Point (GICP) [41] combined with RANSAC [40].

The process begins with Statistical Outlier Removal (SOR) [42], which filters the noise from the raw point clouds by

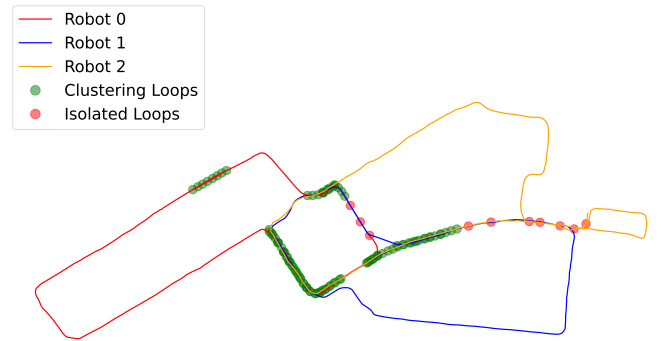


Fig. 3: An example of loop classification, the trajectories of multi-robot and the two types of loops are shown in the figure.

analyzing the statistical distribution of point-to-neighbor distances. GICP is then employed to align the filtered point clouds, initialized using the transformation estimated by RING++. To validate the alignment, correspondences between the two point clouds are refined using a RANSAC-based correspondence rejection method, which discards outliers inconsistent with rigid transformations. The loop is accepted only if the number of inlier correspondences exceeds a predefined threshold. Additionally, the GICP fitness score is used as a quantitative metric for alignment quality—alignments with poor scores or non-convergence are discarded. This two-stage filtering approach significantly enhances the reliability of loop closures by ensuring that only geometrically valid alignments are retained.

#### Loop Classification.

Following the outlier rejection process, the remaining valid loop closures are classified to facilitate efficient spatial bundle adjustment. Specifically, we categorize loops into two types

based on their spatial distribution: clustered loops and isolated loops.

We implement a region-growing algorithm based on Breadth-First Search (BFS). Starting from the spatial center of each loop, the algorithm incrementally searches for nearby loops within a predefined radius. If neighboring loops are found, the search expands from their centers, continuing recursively until no additional nearby loops are detected. Loops that form such spatial clusters are labeled as clustered loops, while those without adjacent loops are marked as isolated loops. An illustrative example of this classification process is shown in Fig. 3.

### Loop Recall.

Since the outlier rejection step adopts strict criteria to ensure robustness and accuracy, it may inadvertently discard valid loop closures as, resulting in false negatives. These missing constraints between robot trajectories hinder the correction of divergence in overlapping areas, potentially degrading the consistency of the fused multi-robot map.

To address this issue, we propose a loop recall mechanism to recover previously discarded valid loops. After the first pose graph optimization (Section III-D) aligns all robot trajectories into the same coordinate system using correct loops, the updated poses are used to re-evaluate previously rejected loops. If the Euclidean distance between the associated poses is below a threshold (2 meters in our system), the loop is recalled for further optimization. This lightweight and distance-based strategy effectively recovers useful constraints and enhances subsequent optimization.

### C. Spatial Bundle Adjustment

Traditional bundle adjustment methods [23]–[25] jointly optimize sequential poses within a sliding window of temporally ordered data. However, they struggle with scenarios involving revisiting the same location over long time spans, making them unsuitable for multi-robot systems. Different from previous BA methods, our spatial bundle adjustment operates within spatially localized windows, jointly optimizing poses from different robots in overlapping regions simultaneously. This design effectively reduces map divergence across sessions, as demonstrated in Fig.4 and Fig.9. Our approach specifically focuses on loop closure regions for two reasons: (1) these regions often exhibit significant spatial overlap among submaps and suffer from high divergence; (2) they contain multiple observations of the same geometric structure from different times or agents, offering rich constraints for accurate joint optimization.

The spatial bundle adjustment is performed on all correct loops after the first pose graph optimization and the loop recall step. All available loops are divided into two categories based on the principle of loop classification in Section III-B. The poses of all robots after FPGO are built into a kd-tree using their spatial positions for faster searching. For each loop, we define a spherical spatial window centered at the midpoint between the two poses involved in the loop. Within this window, all nearby poses are included in the spatial bundle adjustment. For faster searching, we employ a radius-based search using the pose kd-tree to efficiently retrieve the

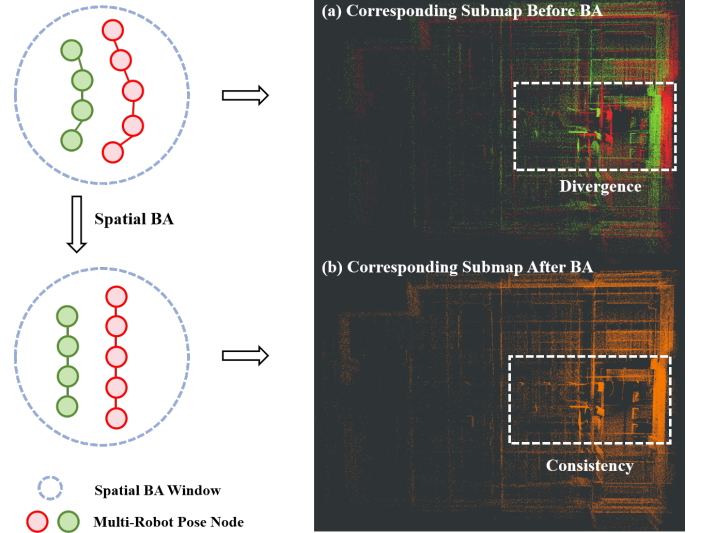


Fig. 4: The red and green nodes in the left part show the trajectories of different robots at certain loop. (a) and (b) show the submaps before BA optimization and after BA optimization respectively. Our spatial bundle adjustment significantly reduces divergence and generates locally consistent map.

poses in the spherical region. These selected poses form the local optimization window for the spatial bundle adjustment, ensuring that only the spatially correlated data around the loop are refined. Depending on the type of loop closure classified in Section III-B, we propose two forms of spatial bundle adjustment designed for their respective characteristics. For isolated loops, we apply our developed spatial diffusion bundle adjustment (DBA). For clustered loops, a spatial variant of the hierarchical bundle adjustment (HBA) [25] is proposed.

#### DBA for isolated loops.

Our DBA is built upon BALM2 [24], which jointly optimizes poses by minimizing the distances from feature points to the corresponding planes. However, BALM, which relies on accurate initial plane estimation, struggles or fails to converge reliably when the same plane observed by different robots appears misaligned due to map divergence. In such cases, the same structure may be voxelized as separate multi-layer planes (shown in Fig. 4 (a)), making direct optimization invalid. To address this, we partition the poses within the spatial window by robot into distinct clusters, each with its own point cloud, as illustrated in the left part of Fig.4. We then apply GICP [41] to roughly align these clusters, reducing plane stratification and enabling reliable plane estimation for subsequent optimization.

After the initial pose graph optimization incorporating an isolated loop, the poses near the loop center are effectively aligned and optimized. However, as the distance from the loop center increases, the influence of the loop constraints in FPGO gradually weakens, leading to less accurate optimization and alignment of distant poses. Therefore, for isolated loops, the key point is to figure out how large its influence range is and align the surrounding affected poses. We develop spatial Diffusion Bundle Adjustment (DBA) to tackle this issue.

In DBA, we begin with a set of LiDAR poses confined to a small range near an isolated loop. We then gradually expand

the set by diffusely incorporating additional LiDAR poses from increasingly wider ranges. The key principle is that, within the loop influence region, poses located further from the loop center contribute less accurately to the representation of the loop's features. The details of DBA are as follows:

For simplicity, we use the following notation, and we refer the reader to [24] for more detailed information. In this paper, feature is seen as *point clusters*, denoted by set  $\mathcal{C} = \{\mathbf{p}_k \in \mathbb{R}^3 | k = 1, \dots, n\}$ , and the corresponding *point cluster coordinate*  $\mathfrak{R}(\mathcal{C})$  is defined as:

$$\mathfrak{R}(\mathcal{C}) \triangleq \sum_{k=1}^n \begin{bmatrix} \mathbf{p}_k \\ 1 \end{bmatrix} \begin{bmatrix} \mathbf{p}_k^T & 1 \end{bmatrix} = \begin{bmatrix} \mathbf{P} & \mathbf{v} \\ \mathbf{v}^T & n \end{bmatrix} \in \mathbb{S}^{4 \times 4} \quad (1)$$

$$\mathbf{P} = \sum_{k=1}^n \mathbf{p}_k \mathbf{p}_k^T, \quad \mathbf{v} = \sum_{k=1}^n \mathbf{p}_k$$

A BA formulation with determining LiDAR poses  $\mathbf{T} = (\mathbf{T}_1, \dots, \mathbf{T}_{M_p})$ , where  $M_p$  is the number of poses, and feature parameters  $\boldsymbol{\pi} = (\boldsymbol{\pi}_1, \dots, \boldsymbol{\pi}_{M_f})$ , where  $M_f$  is the number of features, starts with the optimization problem:

$$\min_{\mathbf{T}, \boldsymbol{\pi}} \left( \sum_{i=1}^{M_f} c(\boldsymbol{\pi}_i, \mathbf{T}) \right). \quad (2)$$

When using plane features, each cost item standards for the squared Euclidean distance from a plane, which can be proved (BALM2 [24]) that it is in the form of

$$c_i(\mathbf{T}) = \lambda_3 \left( \mathbf{A} \left( \sum_{j=1}^{M_p} \mathbf{T}_j \mathbf{C}_{f_{ij}} \mathbf{T}_j^T \right) \right) \quad (3)$$

$$\mathbf{A}(\mathbf{C}) \triangleq \frac{1}{N} \mathbf{P} - \frac{1}{N^2} \mathbf{v} \mathbf{v}^T, \quad \mathbf{C} = \begin{bmatrix} \mathbf{P} & \mathbf{v} \\ \mathbf{v}^T & N \end{bmatrix} \in \mathbb{S}^{4 \times 4}$$

with  $\lambda_3(\mathbf{A})$  as the 3rd largest eigen value of matrix function  $\mathbf{A}$ ,  $\mathbf{C}_{f_{ij}} \in \mathbb{R}^{4 \times 4}$  being a pre-computed matrix where

$$\mathbf{C}_{f_{ij}} = \begin{bmatrix} \mathbf{P}_{f_{ij}} & \mathbf{v}_{f_{ij}} \\ \mathbf{v}_{f_{ij}}^T & N_{f_{ij}} \end{bmatrix} \quad (4)$$

$$\mathbf{P}_{f_{ij}} = \sum_{k=1}^{N_{ij}} \mathbf{p}_{f_{ijk}} \mathbf{p}_{f_{ijk}}^T, \quad \mathbf{v}_{f_{ij}} = \sum_{k=1}^{N_{ij}} \mathbf{p}_{f_{ijk}}$$

Leveraging the above definition, where *point clusters* forming plane features, we could solve the problem with an optimal update  $\Delta \mathbf{T}^*$  using the Levenberg-Marquardt (LM) algorithm:

$$\Delta \mathbf{T}^* = -(\mathbf{H} + \mu \mathbf{I})^{-1} \mathbf{J}^T, \quad (5)$$

Here  $\mu$  is the damping parameter, while  $\mathbf{J}$  and  $\mathbf{H}$  are the Jacobian and Hessian of the cost function, respectively.

In DBA, we categorize the poses into  $D$  groups based on their distances from the loop. Each group contains a set of poses. The number of poses in the  $d_i$ -th group is denoted as  ${}^{d_i}M_p$  (for  $i = 0, \dots, D$ ). In the following part, we first demonstrate that in this *incremental* form of BA, the optimal update formulation remains the same as performing BA jointly on all features. We then prove that the algorithmic complexity is slightly smaller compared to the traditional BA methods, and our approach achieves a relatively higher confidence level which should perform better in practice.

In the  $d_i$ -th diffusion process, we treat all poses that participated in the previous  $i$  diffusion process as accurate and freeze their gradients, meaning they are not optimized furthermore. Consequently, when optimizing the  $d_i$ -th process, we can categorize the poses into two groups  ${}^0\mathbf{T}$  and  ${}^1\mathbf{T}$  with numbers of  $M_{p_0} \triangleq \sum_{k=0}^{i-1} {}^{d_k}M_p$  and  $M_{p_1} \triangleq {}^{d_i}M_p$ .

*Lemma 1.* If  $\mathbf{A}(x)$  is a continuous real symmetric matrix function (i.e.,  $\mathbf{A}(x)$  is continuous in  $x$  and is symmetric for every  $x$ ), then its eigenvalue function  $\lambda_i(x)$  is also continuous. *Proof.* See Appendix (V).  $\square$

According to the definition of matrix  $\mathbf{A}$ , we could obviously get  $\mathbf{A}(\mathbf{C}) \in \mathbb{S}^{3 \times 3}$ . Hence, based on Lemma 1, we could easily get every item of cost function is a continuous function. In the formulation of DBA, cost item could be rewritten as:

$$c_i({}^1\mathbf{T}) = \lambda_3 \left( \mathbf{A} \left( \mathbf{K} + \sum_{j_1=1}^{M_{p_1}} {}^1\mathbf{T}_{j_1} \mathbf{C}_{f_{ij_1}} {}^1\mathbf{T}_{j_1}^T \right) \right), \quad (6)$$

where constant  $\mathbf{K} \triangleq \sum_{j_0=1}^{M_{p_0}} {}^0\mathbf{T}_{j_0} \mathbf{C}_{f_{ij_0}} {}^0\mathbf{T}_{j_0}^T$ . While the cost function is continuous, according to the chain rule, the gradient would be:

$$\begin{aligned} \left( \frac{\partial c_i({}^1\mathbf{T})}{\partial {}^1\mathbf{T}} \right) ({}^1\mathbf{T}_0) &\triangleq \left( \frac{\partial c_i({}^1\mathbf{T}_0 \boxplus \delta {}^1\mathbf{T})}{\delta {}^1\mathbf{T}} \right) (0) \\ &= \frac{\partial \lambda_3(\mathbf{A})}{\partial \mathbf{A}} \frac{\partial \mathbf{A}(\cdot)}{\partial (\cdot)} \frac{\partial \left( \mathbf{K} + \sum_{j_1=1}^{M_{p_1}} {}^1\mathbf{T}_{j_1} \mathbf{C}_{f_{ij_1}} {}^1\mathbf{T}_{j_1}^T \right)}{\partial {}^1\mathbf{T}} \\ &= \frac{\partial \lambda_3(\mathbf{A})}{\partial \mathbf{A}} \frac{\partial \mathbf{A}(\cdot)}{\partial (\cdot)} \frac{\partial \left( \sum_{j_1=1}^{M_{p_1}} {}^1\mathbf{T}_{j_1} \mathbf{C}_{f_{ij_1}} {}^1\mathbf{T}_{j_1}^T \right)}{\partial {}^1\mathbf{T}} \\ &= \left( \mathbf{0}_{M_{p_0}} \quad \mathbf{1}_{M_{p_1}} \right) \left( \frac{\partial c_i(\mathbf{T})}{\partial \mathbf{T}} \right) (\mathbf{T}_0) \begin{pmatrix} \mathbf{0}_{M_{p_0}} \\ \mathbf{1}_{M_{p_1}} \end{pmatrix} \end{aligned} \quad (7)$$

where it does not change when optimizing  ${}^1\mathbf{T}$  compared with jointly solving the BA. The same is true for the second-order gradient, so we only need to freeze the update for  ${}^0\mathbf{T}$  poses ( ${}^0\Delta \mathbf{T} = 0$ ). The solver that jointly solves this BA problem has a complexity of  $O(M_f M_p + M_f M_p^2 + M_p^3)$ , while by masking the Jacobian and Hessian flexibly, our DBA could achieve a complexity of:

$$\begin{aligned} &O \left( M_f \sum_{k=0}^i {}^{d_k}M_p + M_f \sum_{k=0}^i {}^{d_k}M_p^2 + \sum_{k=0}^i {}^{d_k}M_p^3 \right) \\ &\leq O(M_f M_p + M_f M_p^2 + M_p^3) \end{aligned} \quad (8)$$

Let us estimate the confidence level of the estimated pose using the covariance estimation. Denote  $\mathbf{C}_f = \{\mathbf{C}_{f_{ij}}\}$ ,  $\delta \mathbf{C}_f = \{\delta \mathbf{C}_{f_{ij}}\}$ , and  $\mathbf{T}^*$  as the converged solution using the measured cluster  $\mathbf{C}_f$ , according to BALM2, we get:

$$\delta \mathbf{T}^* = \mathbf{H}^{-1} \frac{\partial \mathbf{J}^T(\mathbf{T}^*, \mathbf{C}_f)}{\partial \mathbf{C}_f} \delta \mathbf{C}_f \sim \mathcal{N}(\mathbf{0}, \boldsymbol{\Sigma}_{\delta \mathbf{T}^*}), \quad (9)$$

$$\begin{aligned} \boldsymbol{\Sigma}_{\delta \mathbf{T}^*} &= \mathbf{H}^{-1} \frac{\partial \mathbf{J}^T(\mathbf{T}^*, \mathbf{C}_f)}{\partial \mathbf{C}_f} \boldsymbol{\Sigma}_{\delta \mathbf{C}_f} \frac{\partial \mathbf{J}(\mathbf{T}^*, \mathbf{C}_f)}{\partial \mathbf{C}_f} \mathbf{H}^{-T} \\ &= \mathbf{H}^{-1} \left( \sum_{i=1}^{M_f} \sum_{j=1}^{M_p} \mathbf{L}_{ij} \boldsymbol{\Sigma}_{c_{f_{ij}}} \mathbf{L}_{ij}^T \right) \mathbf{H}^{-T}. \end{aligned} \quad (10)$$

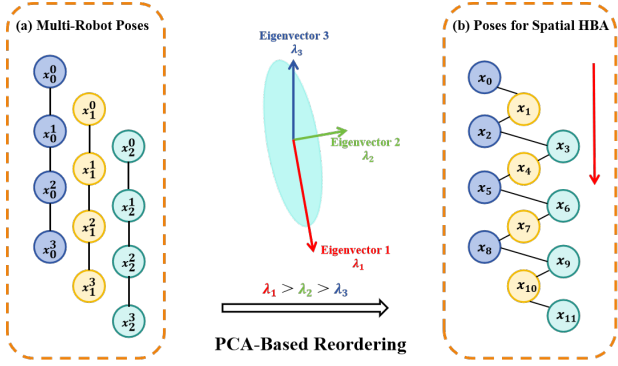


Fig. 5: (a) shows the Multi-robot poses in a spatial window. (b) shows the reordered poses using PCA for HBA.

where

$$\Sigma_{c_{f_{ij}}} = \sum_{k=1}^{N_{ij}} \mathbf{B}_{f_{ijk}} \Sigma_{p_{f_{ijk}}} \mathbf{B}_{f_{ijk}}^T, \mathbf{B}_{f_{ijk}} \in \mathbb{R}^{9 \times 3} \quad (11)$$

$$\frac{\partial \mathbf{J}^T}{\partial c_{f_{ij}}} = \begin{bmatrix} \vdots \\ \frac{\partial (\mathbf{J}^p)^T}{\partial c_{f_{ij}}} \\ \vdots \end{bmatrix} = \begin{bmatrix} \vdots \\ \mathbf{L}_{ij}^p \\ \vdots \end{bmatrix} \triangleq \mathbf{L}_{ij} \in \mathbb{R}^{6M_p \times 9} \quad (12)$$

**Assumption 1.** Small range LiDAR poses  $M_{p_0}$  that participate in the BA have smaller covariance  $\sum_{i=1}^{M_f} \sum_{j=1}^{M_{p_0}} |\Sigma_{c_{f_{ij}}}|$  in measurement noise compared to LiDAR poses  $M_{p_1}$  in wider ranges.

According to Assumption 1, with the previous group categorization, define  ${}^0\mathbf{L}_{ij} \triangleq \mathbf{L}_{ij}[0:6M_{p_0},:]$  and  ${}^1\mathbf{L}_{ij} \triangleq \mathbf{L}_{ij}[6M_{p_0}+1:6M_{p_1},:]$ , we can obtain that:

$$\begin{aligned} \Sigma_{\delta \mathbf{T}^*}^{\text{small}} &= \mathbf{H}^{-1} \left( \sum_{i=1}^{M_f} \left( \sum_{j=1}^{M_{p_0}} {}^0\mathbf{L}_{ij} \Sigma_{c_{f_{ij}}} {}^0\mathbf{L}_{ij}^T \right. \right. \\ &\quad \left. \left. + \sum_{j=1}^{M_{p_1}} {}^1\mathbf{L}_{ij} \Sigma_{c_{f_{ij}}} {}^1\mathbf{L}_{ij}^T \right) \right) \mathbf{H}^{-T} \quad (13) \\ &\leq \mathbf{H}^{-1} \left( \sum_{i=1}^{M_f} \sum_{j=1}^{M_p} \mathbf{L}_{ij} \Sigma_{c_{f_{ij}}} \mathbf{L}_{ij}^T \right) \mathbf{H}^{-T} = \Sigma_{\delta \mathbf{T}^*}. \end{aligned}$$

Thus, under our assumption, fixing the number of iterations yields lower measurement noise, while fixing the confidence level leads to faster convergence.

### HBA for clustered loops.

For two trajectories from different robots with significant overlapping regions, loop closures tend to appear densely, and adjacent loops often share large overlapping areas in their associated point cloud maps. In such clustered loop groups, it is crucial to jointly process the loops within the entire overlapping region to maintain local consistency and optimization accuracy. If we optimize the poses by processing loop closures sequentially and independently rather than jointly, this may introduce inconsistencies and even divergence in overlapping regions due to contradictory constraints. To address this, we adapt and extend HBA [25] into a multi-robot framework for

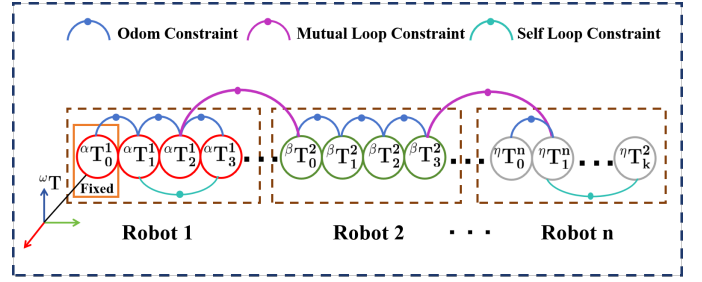


Fig. 6: The first pose graph optimization, with constraints including odometry and loop closure. The first pose of the first robot is fixed as the world coordinate.

clustered loop scenarios.

The original HBA relies on temporally ordered poses from a single robot, assuming adjacent poses share common point cloud features. However, in our multi-robot setting, poses selected via kd-tree radius search within a loop cluster are unordered and from different robots. To address this, we use Principal Component Analysis (PCA) to analyze the spatial distribution of selected poses and reorder them along the principal axis defined by the largest eigenvalue, as illustrated in Fig. 5. This spatial reordering ensures neighboring poses in the optimization sequence are also spatially close, promoting shared features and effective constraints. Once reordered, all poses are processed consistently in a unified optimization window, enabling the enhanced HBA to accurately align the geometry across overlapping regions from multiple robots.

### D. Two-Step Pose Graph Optimization

The two-step pose graph optimization are used to align and refine the global structure of multi-robot trajectories. The details of each step are as follows.

#### First Pose graph optimization (FPGO).

Following loop processing, we perform the first pose graph optimization to coarsely align the trajectories of all robots. We construct a centralized pose graph shown in Fig. 6, in which each robot's pose sequence is included as a subgraph. The graph incorporates three types of constraint: odometry, self-loop, and inter-loop. The first pose of the first robot is fixed to define the origin point of the world coordinate, ensuring that all other robot trajectories are aligned to this global reference frame. With this initial alignment established, we acquire a rough estimate of the relative positions among all robot trajectories, which enables us to recover the valid but previously rejected loops (in Section III-B).

#### Last Pose Graph Optimization (LPGO).

Although spatial BA (Section III-C) improves the accuracy of local pose near loop closures, it does not propagate this accuracy globally and may break the continuity of odometry, resulting in even worse global consistency. We develop the last pose graph optimization to address this, and the details are as follows.

To achieve global consistency while preserving local accuracy, we design the final pose graph optimization with two types of constraints: odometry constraints to maintain trajectory smoothness, sparsified BA-based constraints to preserve

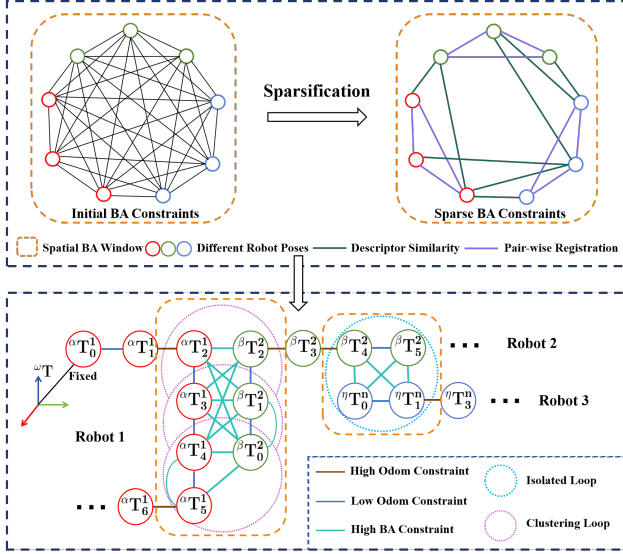


Fig. 7: The upper part of the picture shows the sparsification of BA constraints in a spatial window at loop. The sparse BA constraints are added to pose graph below along with odometry constraints.

refined local structures (see Fig. 7). For each robot, odometry constraints are added between adjacent poses to preserve temporal continuity. In cases where a BA-optimized pose is adjacent to an under-optimized one, a high-weight odometry constraint is applied to mitigate potential discontinuity introduced by local optimization. Conversely, lower weights are assigned between under-optimized poses to allow greater global adjustment flexibility. Additionally, pose pairs within the spatial BA window that exhibit strong geometric overlap and reliable correspondence are assigned high-weight BA constraints to preserve local accuracy. The specific selection criteria for these constraints are detailed in the following paragraphs.

We use two different metrics for constraint selection between pose pairs of different robots and pose pairs of the same robot. For pose pairs across different robots, we evaluate the similarity of their descriptors obtained from RING++ [21] and add BA constraints only when the similarity exceeds a specified threshold. For pose pairs within the same robot, we apply pairwise registration techniques from [43] to selectively retain constraints between poses that significantly restrain each other. The sparsification process using pairwise registration is as follows.

For an edge  $\mathbf{E}_k$  between two pose nodes, the  $\mathbf{E}_k^0$ -th pose and the  $\mathbf{E}_k^1$ -th pose, of the same robot. The relative pose residual ( $\epsilon_k$ ) and covariance ( $\Omega_k$ ) between these poses can be approximated using the pairwise registration formulation. The  $\mathbf{E}_k^0$ -th pose and the  $\mathbf{E}_k^1$ -th pose are denoted as  $\mathbf{R}_{L_0}, \mathbf{t}_{L_0}$  and  $\mathbf{R}_{L_1}, \mathbf{t}_{L_1}$  respectively for convenience. The relative pose is denoted as  $\mathbf{R}_{L_1}^T \mathbf{R}_{L_0}, \mathbf{t}_{L_1}^T \mathbf{t}_{L_0} = \mathbf{R}_{L_0}^T (-\mathbf{t}_{L_0} + \mathbf{t}_{L_1})$ . Utilizing nearest searching and taking the point-to-point correspondences  $\{(\mathbf{P}_u^{L_0}, \mathbf{P}_u^{L_1})\}_{u=1}^U$  as input, the registration function  $\epsilon_k^{\text{reg}}$  for  $\mathbf{E}_k$  is as follows.

$$\epsilon_k^{\text{reg}} = \sum_{u=1}^U (\mathbf{R}_{L_1}^{L_0} \mathbf{P}_u^{L_1} + \mathbf{t}_{L_1}^{L_0} - \mathbf{P}_u^{L_0}), \quad (14)$$

TABLE I: OVERVIEW OF SELF-COLLECTED DATASET

Dataset	Environment	Trajectory Length (m)	LiDAR
Garage	Indoor	334	Mid360
Library	Outdoor	519	Mid360
Yard	Indoor & Outdoor	232	Mid360
Laboratory	Indoor & Outdoor	98	Mid360

The Jacobian of  $\epsilon_k^{\text{reg}}$  respect to the relative pose  $\mathbf{R}_{L_1}^{L_0}, \mathbf{t}_{L_1}^{L_0}$  is calculated by (15).

$$\mathbf{J}_k^{\text{reg}} = \sum_{u=1}^U \begin{bmatrix} -[\mathbf{P}_u^{L_0}]_{\times} & \mathbf{0} \\ \mathbf{0} & \mathbf{I} \end{bmatrix}. \quad (15)$$

The covariance  $\Omega_k$  of the registration function  $\epsilon_k^{\text{reg}}$  is calculated as follows.

$$\Omega_k = \mathbf{J}_k^{\text{reg}T} \mathbf{J}_k^{\text{reg}}. \quad (16)$$

The minimal eigen value of the covariance  $\lambda_k^{\min} = \lambda_{\min}(\Omega_k)$  can be used to represent the constraint ability of the point cloud from  $\mathbf{E}_k^0$ -th pose and  $\mathbf{E}_k^1$ -th pose. When the  $\lambda_{\min}(\Omega_k)$  of two node is small enough, the BA constraint between them will be retained and added to the pose graph in Fig. 7. On the contrary, no constraints from BA will be added between  $\mathbf{E}_k^0$ -th pose and  $\mathbf{E}_k^1$ -th pose with a relatively large  $\lambda_{\min}(\Omega_k)$  value.

## IV. EXPERIMENTS

### A. Experimental Setup

All algorithms are implemented in C++ using the Robot Operating System (ROS). To evaluate the performance of the proposed multi-session map merging framework, we conduct experiments on several datasets, including the publicly available S3E [44], GEODE [45], MARS-LVIG [1], R<sup>3</sup>LIVE [46] dataset, as well as a self-collected dataset. The GEODE, MARS-LVIG and R<sup>3</sup>LIVE datasets are segmented into multiple sessions with overlapping areas, but the starting point of each part is different and the relative transformation is unknown. The parameters of the public datasets and our self-collected dataset are shown in Table II and Table I, respectively. For all public datasets, initial odometry is obtained using the LiDAR-Inertial Odometry method recommended by the respective dataset, while the initial odometry for our own dataset is generated using FAST-LIO2 [14].

We first evaluate our proposed spatial bundle adjustment by comparing it against the conventional LiDAR-based bundle adjustment methods BALM2 [24] and HBA [25] (Section IV-B). Next, we assess the performance of our complete multi-session merging framework against DCL-SLAM [27] and LAMM [29] (Section IV-C). An ablation study is then conducted to analyze the contributions of individual components within our framework (Section IV-D). Finally, we test the scalability of our method in handling a large number of sessions (Section IV-E).

TABLE II: OVERVIEW OF OPEN DATASET

Dataset	Sequence	Robot Num	Traj Length (m)	LiDAR
S3E	Campus_1	3	2989	Velodyne
	Campus_3	3	2938	Velodyne
	Dormitory	3	2168	Velodyne
	Library	3	1524	Velodyne
	Teaching_Building	3	1983	Velodyne
	Tunnel	3	1525	Velodyne
GEODE	Inlandwaterways	3	1209	Avia
	Tunnelingtunnel	3	270	Avia
	Stairs	2	161	Ouster
LVIG	Airport	2	4135	Avia
	Valley	3	6697	Avia
	Town	4	6117	Avia
	Island	2	2139	Avia
R <sup>3</sup> LIVE	HKU Park	5	356	Avia
	HKU Campus	10	338	Avia
	HKU Mainbuilding	20	945	Avia

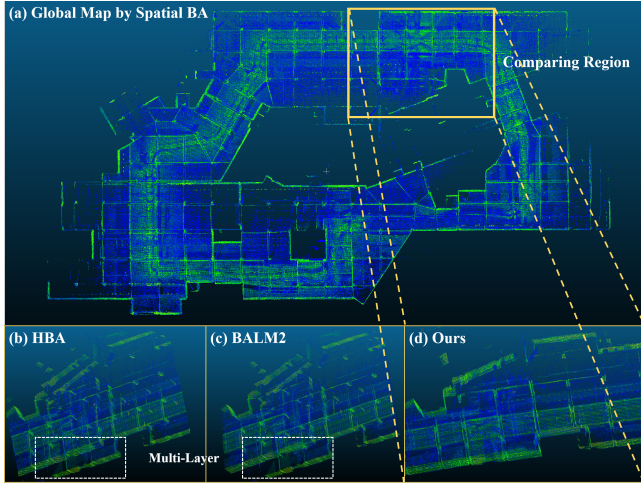


Fig. 8: Result of single robot study. (a) shows the global map generated by our method. (b)-(d) shows the details of the local map at loop.

### B. Single-Robot Study

To evaluate the effectiveness of our spatial bundle adjustment (BA), we utilize our self-collected single-robot dataset consisting of several indoor and outdoor scenes (Table I). During data acquisition, the  $z$ -axis value remains largely stable across each scene, allowing it to serve as a reference to evaluate vertical drift.

Each sequence in our dataset includes loop closures that enable spatial BA (Section III-C). We compare our spatial BA with BALM2 [24] and HBA [25], using average  $z$ -axis drift ( $z$ -DRIFT) and  $z$ -axis Root Mean Square Error ( $z$ -RMSE) as primary evaluation metrics. Both metrics are computed with respect to the  $z$ -value of the first frame as a reference, allowing a consistent evaluation of vertical alignment over time. Due to the absence of ground truth, we also compute the Mean Map Entropy (MME) using MapEval [47], where lower values indicate better map consistency and reduced clutter. To ensure a fair comparison of the performance of the three BA methods, all methods are evaluated using raw odometry trajectories

TABLE III: MME,  $z$ -DRIFT AND  $z$ -RMSE OF SINGLE ROBOT STUDY

Scene	Method	MME	$z$ -Drift	$z$ -RMSE
Garage	HBA	-6.83	5.98	7.14
	BALM2	<b>-6.93</b>	5.95	7.17
	Ours	-6.86	<b>4.87</b>	<b>5.35</b>
Library	HBA	-5.95	6.17	6.78
	BALM2	-6.20	6.51	7.31
	Ours	<b>-6.23</b>	<b>3.68</b>	<b>4.53</b>
Yard	HBA	-6.39	2.33	2.70
	BALM2	-5.93	1.86	2.12
	Ours	<b>-6.40</b>	<b>1.12</b>	<b>1.25</b>
Laboratory	HBA	<b>-6.26</b>	3.24	3.72
	BALM2	-6.04	3.22	3.70
	Ours	-6.20	<b>3.17</b>	<b>3.64</b>

TABLE IV: RMSE OF THE ATE(m) OF OPEN DATASET

Scene	DCL-SLAM	LAMM	Ours
Campus_3	17.89	12.51	<b>3.51</b>
Dormitory	3.52	28.67	<b>3.46</b>
Library	6.37	4.58	<b>1.48</b>
Tunnel	3.09	×	<b>0.99</b>
Inlandwaterways	×	×	<b>7.44</b>
Offroad	×	25.45	<b>1.30</b>
Tunnelingtunnel	×	0.62	<b>0.16</b>
Airport	×	8.41	<b>1.30</b>
Town	×	×	<b>1.49</b>
Island	×	×	<b>0.801</b>

without any prior loop-based refinement. For computational feasibility in large-scale scenes, BALM2 is executed in a sliding-window configuration.

Table III presents the results. Our method achieves the best performance across all metrics in the Library and Yard scenarios. Furthermore, it consistently outperforms BALM2 and HBA in  $z$ -DRIFT and  $z$ -RMSE, demonstrating its superior capability in mitigating global drift.

### C. Multi-Robot Study

To further evaluate the proposed framework, we perform comparative multi-robot experiments using the MARS-LVIG [1], GEODE [45], and multi-robot S3E [44] datasets. The parameters of the multi-robot datasets used here are summarized in Table II. Our framework is compared with the multi-robot SLAM system DCL-SLAM [27] and the multi-session map merging method LAMM [29].

The accuracy of map merging is evaluated using the Root Mean Square Error (RMSE) of the Absolute Trajectory Error (ATE). A failure is defined as any sequence with an RMSE greater than 30 meters and is indicated by “×” in the table. As shown in Table IV, the best values are highlighted in bold. Our framework successfully merges all sequences, while LAMM and DCL-SLAM fail in four and six sequences, respectively. In successful cases, our framework achieves significantly lower RMSE values, indicating higher merging accuracy.

We select a scene where all three methods successfully merge the multi-robot point cloud for display. Figure 9 visualizes the results from the S3E Library sequence. The left image

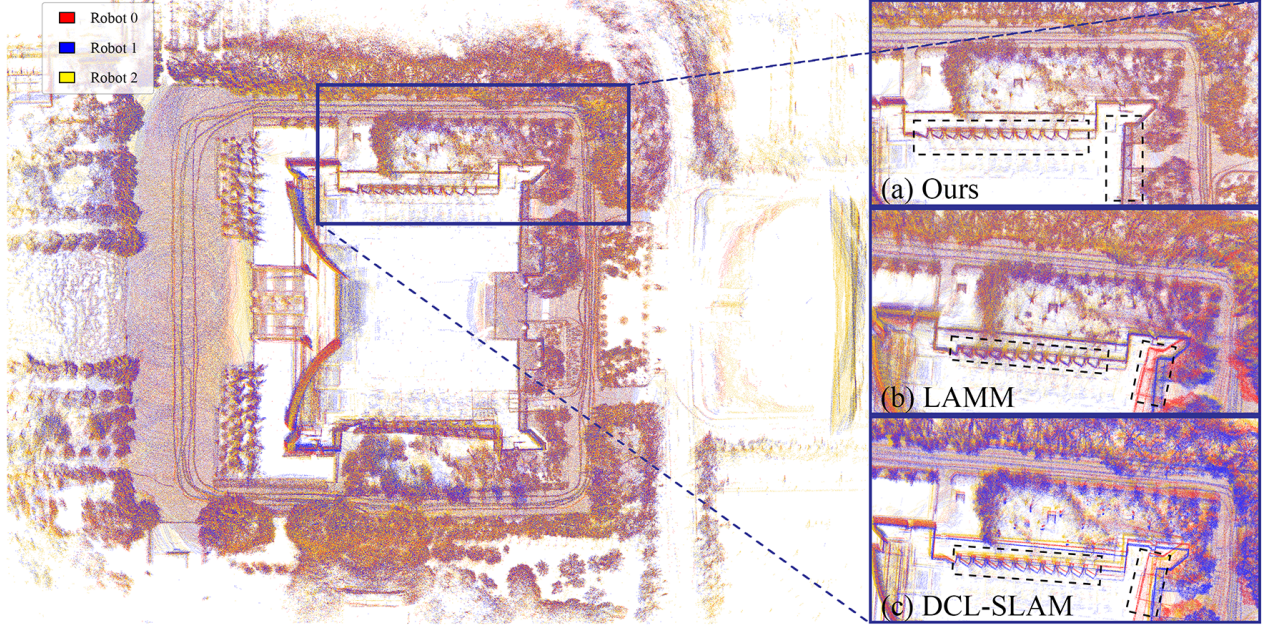


Fig. 9: The map merging result of the S3E library. The local maps generated by three methods are selected for comparison. Our method almost eliminates the divergence of local multi-session point cloud maps. While LAMM [29] and DCL-SLAM [27] suffer from serious inconsistencies.

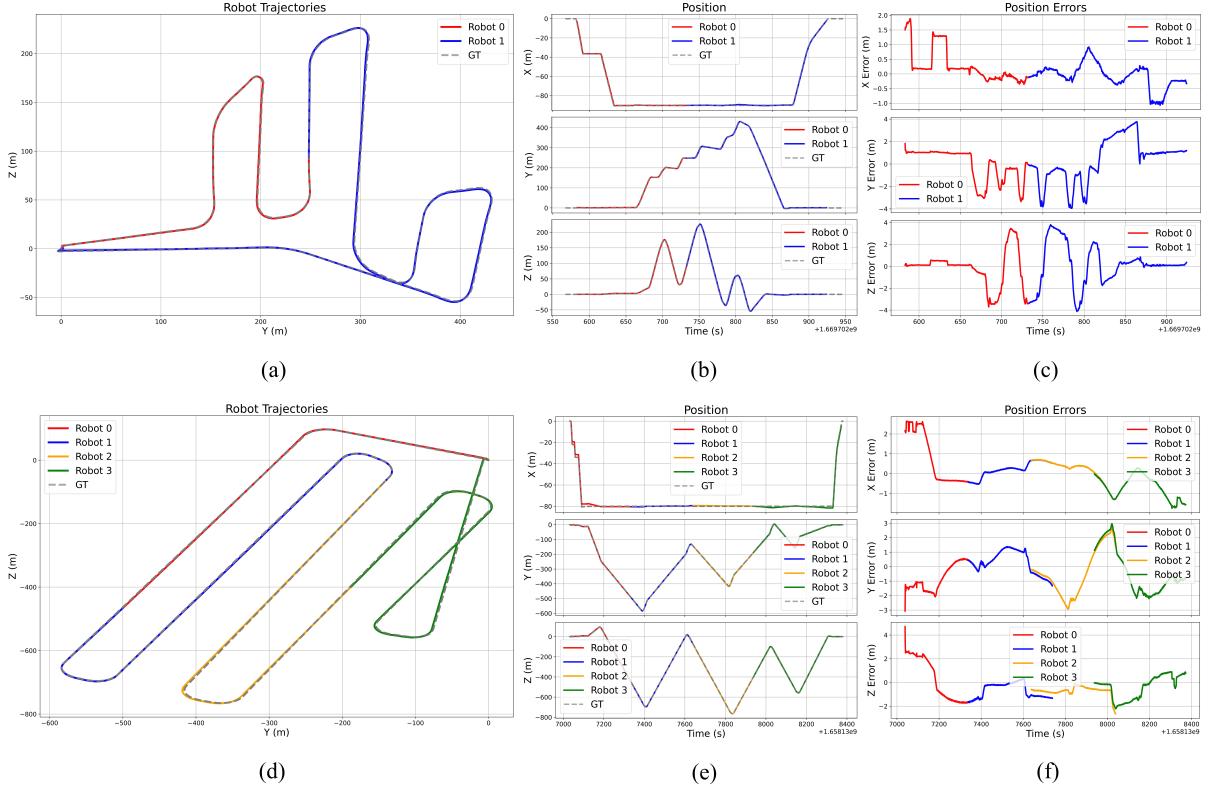


Fig. 10: The optimized trajectory, position, and position error for proposed method in Island ((a)-(c)) and Town ((d)-(f)).

shows our globally consistent and accurate merged map, while the right part shows the local map fusion of the three methods and the comparison of their respective trajectories. Our method yields tightly aligned local maps, whereas LAMM and DCL-

SLAM exhibit severe local divergences. The comparison of trajectory and ground truth further confirms the superior accuracy of our method. Fig. 11 and Fig. 12 present multi-robot trajectories comparisons between our method, LAMM,

TABLE V: LOOP CLOSURE RECALL DATA

Scene	Initial	After Rejection	After Recalling	RMSE <i>w/o</i> LR	RMSE <i>w/</i> LR
Campus_1	225	185	190	9.98	<b>9.97</b>
Dormitory	106	76	77	4.15	<b>4.12</b>
Library	286	235	238	1.41	<b>1.40</b>
Tunnel	208	182	194	1.40	<b>1.29</b>

TABLE VI: ABLATION STUDY RESULTS

Scene	FPGO	FPGO + BA	Lemon Full
Campus_1	9.97	10.05	<b>9.94</b>
Campus_3	3.82	4.26	<b>3.51</b>
Dormitory	4.12	4.40	<b>3.46</b>
Tunnel	1.29	1.52	<b>0.98</b>
Stairs	0.194	0.191	<b>0.142</b>
Valley	7.84	7.39	<b>6.76</b>
Island	0.963	1.076	<b>0.801</b>

and DCL-SLAM. The trajectories estimated by our method closely follow the ground truth for each robot, exhibiting low and stable errors. In contrast, the benchmark methods show significant deviations from the ground truth in some regions and minor local inconsistencies in others. The large deviations are likely caused by incorrect loop closures, while the local inconsistencies may result from the lack of bundle adjustment, which fails to eliminate the divergence of submaps.

The performance disparity can be attributed to LAMM and DCL-SLAM relying solely on PGO with loop closure constraints. Although this achieves general global consistency, it often neglects the refinement of overlapping local regions. Lack of attention to the geometric structure of point cloud maps leads to serious local multi-robot map divergence. Our framework explicitly re-examines the role of loop and enhances its utilization by performing spatial bundle adjustment in local regions, while propagating the refined results globally via the last pose graph optimization. This process effectively reduces divergence and ensures consistent multi-session map fusion. Figure 10 shows optimized trajectories and error plots for different scenes, the multi-robot trajectories generated by our framework are basically consistent with the ground truth, and the error is stable and small, further demonstrating the superior performance and stability of our method.

#### D. Ablation Study

To understand the contribution of each component in our framework, we perform ablation experiments on the S3E, GEODE, and MARS-LVIG datasets. Our ablation experiment consists of two parts.

First, we conduct an ablation experiment on the loop recall module in III-B. We compare the performance of the first pose graph optimization with and without loop recall (LR) using RMSE of the ATE (m), reported in the table as “RMSE *w/* LR” and “RMSE *w/o* LR,” respectively. Because the S3E dataset contains a large number of complex scenes that combine unstructured and structured data, as well as many scenes with high similarity, it is easy to have a large number of false loops, so we use it as the ablation dataset for loop recall.

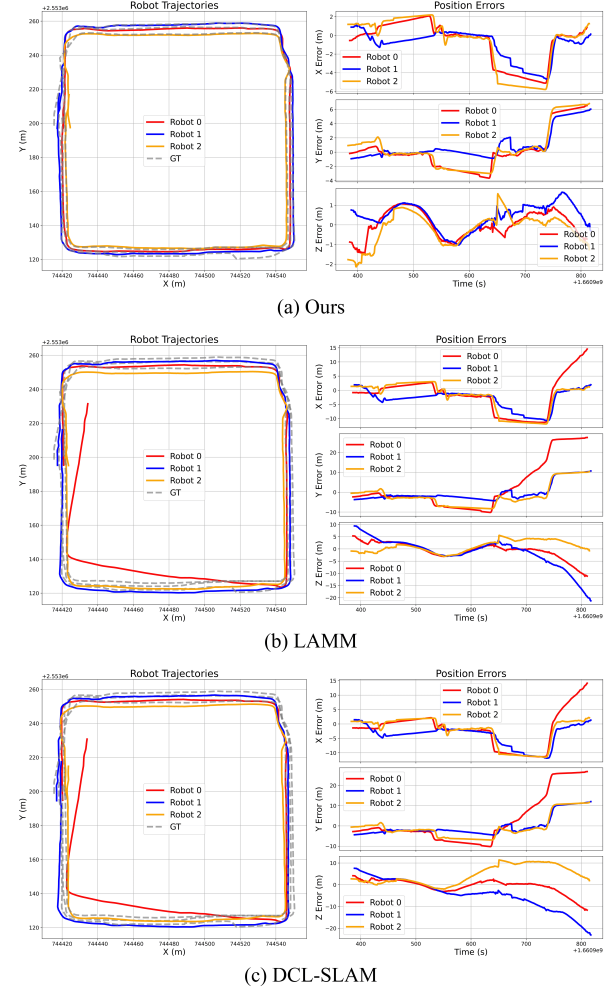


Fig. 11: Comparison of multi-robot trajectories and error plots between our method, LAMM, and DCL-SLAM on the S3E Library dataset. The ground truth is shown as a dashed line in the figure.

Table V shows the number of loops in different loop processing stages, as well as the results of the first pose graph optimization with and without loop recall. The experimental results show that the first PGO achieves smaller errors and better performances when the mistakenly rejected loops are recalled. Beyond its impact on PGO, loop recall also introduces additional constraints that benefit subsequent bundle adjustment.

Second, we evaluate the performance of three variants in our map merging module: (1) First Pose Graph Optimization only (FPGO), (2) First Pose Graph Optimization and Spatial Bundle Adjustment (FPGO + BA) and (3) the full Lemon-Mapping system (Lemon Full). RMSE of the ATE (m) is used for quantitative comparison.

Table VI summarizes the results, with the best values highlighted in bold. The complete framework consistently achieves the lowest RMSE, validating the effectiveness of combining local BA and two PGO steps. For the variant of FPGO + BA, although local BA improves relative accuracy, it may disrupt the continuity of odometry since it only refines loop regions. Consequently, its standalone use can increase

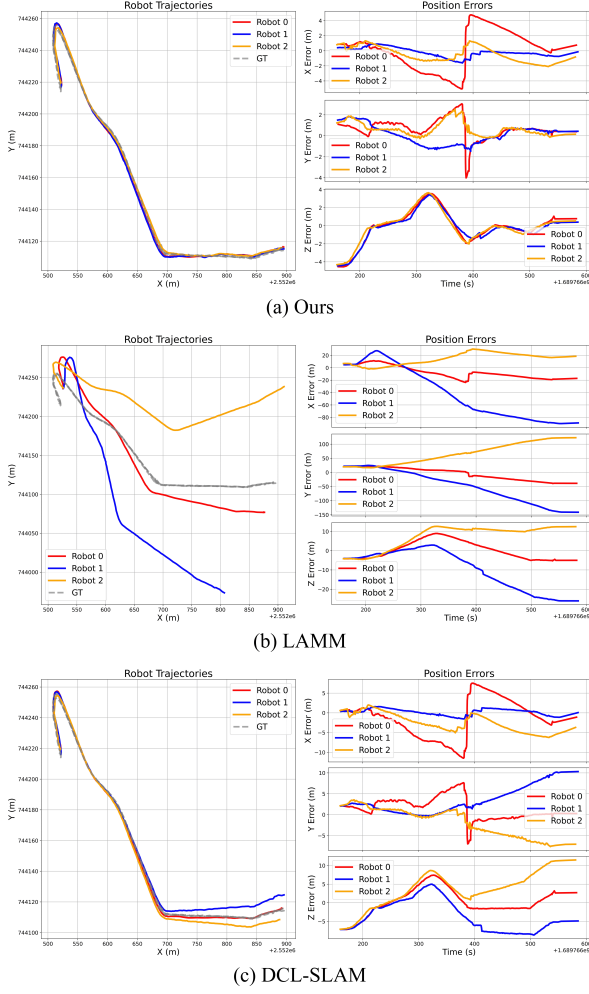


Fig. 12: Comparison of multi-robot trajectories and error plots between our method, LAMM, and DCL-SLAM on the S3E Tunnel dataset. The ground truth is shown as a dashed line in the figure.

TABLE VII: SCALABILITY STUDY RESULTS

Dataset	Robot Num	Merged Num	Success Rate
HKU Park	5	5	<b>100%</b>
HKU Campus	10	10	<b>100%</b>
HKU Mainbuilding	20	18	<b>90%</b>

RMSE compared to FPGO alone. However, the final PGO integrates both local BA constraints and odometry continuity, propagating local accuracy to the global map and significantly reducing RMSE.

Fig. 13 shows that merging maps of three variants above. (a) and (b) demonstrate the function of spatial bundle adjustment to improve local consistency and accuracy compared to PGO only. (c) and (d) in Fig. 13 further illustrates that maps refined with both BA and last pose graph optimization have better global consistency than using BA alone, confirming the role of last PGO in maintaining global map structure.

#### E. Scalability Study

Most existing map fusion frameworks are limited to scenarios involving only a few robots (less than three), and their

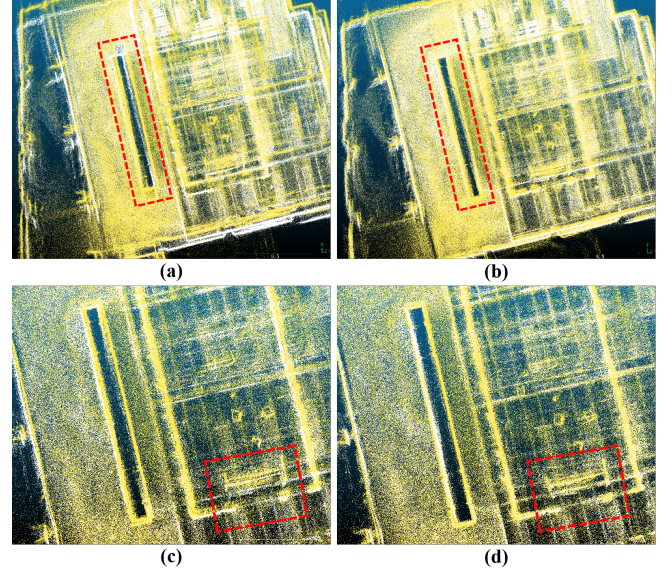


Fig. 13: Result of ablation study. (a) and (b) show the merging map of FPGO and FPGO with BA. (c) and (d) show the merging map of FPGO with BA and Lemon mapping full model. The comparison regions are framed in red.

scalability to large-scale deployments remains unproven. To assess the scalability of our proposed framework, we conduct experiments on the R<sup>3</sup>LIVE dataset, which we subdivide into groups of 5, 10, and 20 sessions. A successful fusion is defined as the correct alignment of each session with all its adjacent sessions that shares sufficient map overlap.

Table VII summarizes the corresponding results of three cases. Our framework achieves a 100% success rate in the 5-session and 10-session scenarios. In the more challenging 20-session case, a single failure occurred since its associated loop is not detected, resulting in a success rate of 90%. These results demonstrate the scalability and robustness of the Lemon-Mapping system when dealing with large numbers of multi-robot map merging.

Fig. 14 visualizes the fused map for the 5-session case of HKU Park in R<sup>3</sup>LIVE dataset, including a global point cloud map from a bird's eye view (BEV) and 6 enlarged map details. The five-session map shows good fusion effect and local accuracy in both structured and unstructured environments.

#### V. CONCLUSION

This paper presents **LEMON-Mapping**, a Loop-Enhanced Large-Scale Multi-Session Point Cloud Merging and OptimizationN framework for Globally Consistent Mapping. Lemon-Mapping is a scalable framework for large number of robots. Unlike existing methods that rely solely on pose sequences, it enhances the role of loop closures by directly utilizing geometric constraints from overlapping point clouds and reasonably transferring the local accuracy to the global map. The framework includes a loop processing module for reliable loop selection and innovate loop recall, and a map merging module that combines two-step pose graph optimization with a spatial bundle adjustment tailored for multi-robot systems. The spatial bundle adjustment operates

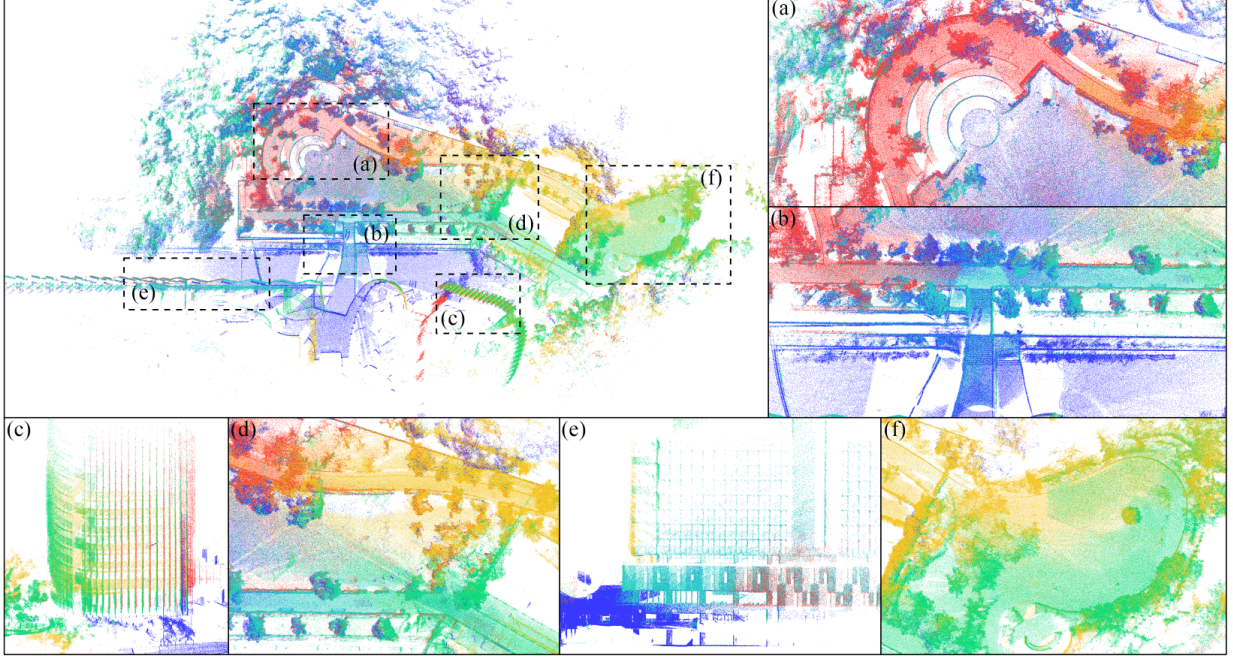


Fig. 14: The map merging result of five sessions in the R<sup>3</sup>LIVE HKU Park dataset. The local maps of (a)-(f) are enlarged to show the details.

on loop-based spatial windows, allowing geometry-aware pose optimization across unordered and cross-robot trajectories. To ensure global consistency, we sparsify the BA constraints and propagate local accuracy across the entire map using a refined pose graph optimization strategy. Experimental results on S3E, MARS-LVIG, GEODE, R<sup>3</sup>LIVE and our self-collected dataset demonstrate that our approach maintains high success rates and robustness as the number of sessions increases, while outperforming traditional methods in geometric accuracy and scalability.

#### APPENDIX: PROOF OF LEMMA 1

Since each  $\mathbf{A}(x)$  is real symmetric, the spectral theorem guarantees an orthogonal matrix  $\mathbf{Q}(x)$  and a real diagonal matrix

$$\mathbf{\Lambda}(x) = \text{diag}(\lambda_1(x), \dots, \lambda_n(x))$$

such that

$$\mathbf{A}(x) = \mathbf{Q}(x) \mathbf{\Lambda}(x) \mathbf{Q}(x)^\top.$$

In particular, the eigenvalues  $\lambda_i(x)$  are all real.

Consider the characteristic polynomial

$$p_x(t) = \det(\mathbf{A}(x) - t \mathbf{I}).$$

On one hand, by orthogonal diagonalization,

$$p_x(t) = \det(\mathbf{\Lambda}(x) - t \mathbf{I}) = \prod_{i=1}^n (\lambda_i(x) - t).$$

On the other hand, expanding the determinant in terms of the entries of  $\mathbf{A}(x)$  shows

$$p_x(t) = t^n + c_{n-1}(x) t^{n-1} + \dots + c_1(x) t + c_0(x),$$

where each coefficient  $c_k(x)$  is a finite sum of products of the entries of  $\mathbf{A}(x)$ . Since  $\mathbf{A}(x)$  is continuous in  $x$ , each  $c_k(x)$  is a continuous function of  $x$ .

By the fundamental theorem of algebra and the fact that all roots of  $p_x$  are real, we may label them in nondecreasing order

$$\lambda_1(x) \leq \lambda_2(x) \leq \dots \leq \lambda_n(x).$$

A standard result on the continuous dependence of polynomial roots on coefficients now implies that each ordered root  $\lambda_i(x)$  varies continuously with the coefficients  $\{c_k(x)\}$ , and hence with  $x$  itself. Therefore every eigenvalue function  $x \mapsto \lambda_i(x)$  is continuous.

## REFERENCES

- [1] H. Li, Y. Zou, N. Chen, J. Lin, X. Liu, W. Xu, C. Zheng, R. Li, D. He, F. Kong *et al.*, “Mars-lvig dataset: A multi-sensor aerial robots slam dataset for lidar-visual-inertial-gnss fusion,” *The International Journal of Robotics Research*, vol. 43, no. 8, pp. 1114–1127, 2024.
- [2] Y. Ren, F. Zhu, G. Lu, Y. Cai, L. Yin, F. Kong, J. Lin, N. Chen, and F. Zhang, “Safety-assured high-speed navigation for mavs,” *Science Robotics*, vol. 10, no. 98, p. eado6187, 2025.
- [3] F. Zhu, Y. Ren, F. Kong, H. Wu, S. Liang, N. Chen, W. Xu, and F. Zhang, “Swarm-liv: Decentralized swarm lidar-inertial odometry,” in *2023 IEEE International Conference on Robotics and Automation (ICRA)*, 2023.
- [4] F. Zhu, Y. Ren, L. Yin, F. Kong, Q. Liu, R. Xue, W. Liu, Y. Cai, G. Lu, H. Li, and F. Zhang, “Swarm-liv2: Decentralized efficient lidar-inertial odometry for aerial swarm systems,” *IEEE Transactions on Robotics*, 2025.
- [5] Y. Cui, R. Chen, W. Chu, L. Chen, D. Tian, Y. Li, and D. Cao, “Deep learning for image and point cloud fusion in autonomous driving: A review,” *IEEE Transactions on Intelligent Transportation Systems*, 2022.
- [6] Y. Ren, Y. Cai, F. Zhu, S. Liang, and F. Zhang, “Rog-map: An efficient robocentric occupancy grid map for large-scene and high-resolution lidar-based motion planning,” in *2024 IEEE/RSJ International Conference on Intelligent Robots and Systems (IROS)*, 2024.
- [7] F. Yang, C. Wang, C. Cadena, and M. Hutter, “iplanner: Imperative path planning,” *Proceedings of Robotics: Science and System XIX*, p. 064, 2023.
- [8] P. Roth, J. Nubert, F. Yang, M. Mittal, and M. Hutter, “Viplanner: Visual semantic imperative learning for local navigation,” in *2024 IEEE International Conference on Robotics and Automation (ICRA)*, 2024, pp. 5243–5249.
- [9] J. Scherer, S. Yahyanejad, S. Hayat, E. Yanmaz, T. Andre, A. Khan, V. Vukadinovic, C. Bettstetter, H. Hellwagner, and B. Rinner, “An autonomous multi-uav system for search and rescue,” in *Proceedings of the first workshop on micro aerial vehicle networks, systems, and applications for civilian use*, 2015, pp. 33–38.
- [10] A. G. Araújo, C. A. Pizzino, M. S. Couceiro, and R. P. Rocha, “A multi-drone system proof of concept for forestry applications,” *Drones*, vol. 9, no. 2, p. 80, 2025.
- [11] T. Rouček, M. Pecka, P. Čížek, T. Petříček, J. Bayer, V. Šalanský, D. Heřt, M. Petrlik, T. Bába, V. Spurný *et al.*, “Darpa subterranean challenge: Multi-robotic exploration of underground environments,” in *Modelling and Simulation for Autonomous Systems: 6th International Conference, MESAS 2019, Palermo, Italy, October 29–31, 2019, Revised Selected Papers 6*. Springer, 2020, pp. 274–290.
- [12] J. Zhang, S. Singh *et al.*, “Loam: Lidar odometry and mapping in real-time,” in *Robotics: Science and systems*, vol. 2, no. 9. Berkeley, CA, 2014, pp. 1–9.
- [13] T.-M. Nguyen, D. Duberg, P. Jensfelt, S. Yuan, and L. Xie, “Slic: Multi-input multi-scale surfel-based lidar-inertial continuous-time odometry and mapping,” *IEEE Robotics and Automation Letters*, vol. 8, no. 4, pp. 2102–2109, 2023.
- [14] W. Xu, Y. Cai, D. He, J. Lin, and F. Zhang, “Fast-liv2: Fast direct lidar-inertial odometry,” *IEEE Transactions on Robotics*, vol. 38, no. 4, pp. 2053–2073, 2022.
- [15] C. Bai, T. Xiao, Y. Chen, H. Wang, F. Zhang, and X. Gao, “Faster-liv: Lightweight tightly coupled lidar-inertial odometry using parallel sparse incremental voxels,” *IEEE Robotics and Automation Letters*, vol. 7, no. 2, pp. 4861–4868, 2022.
- [16] K. Chen, R. Nemiroff, and B. T. Lopez, “Direct lidar-inertial odometry: Lightweight liv with continuous-time motion correction,” in *2023 IEEE international conference on robotics and automation (ICRA)*. IEEE, 2023, pp. 3983–3989.
- [17] D. He, W. Xu, N. Chen, F. Kong, C. Yuan, and F. Zhang, “Point-liv: Robust high-bandwidth light detection and ranging inertial odometry,” *Advanced Intelligent Systems*, vol. 5, no. 7, p. 2200459, 2023.
- [18] R. Kümmerle, G. Grisetti, H. Strasdat, K. Konolige, and W. Burgard, “G2o: A general framework for graph optimization,” in *2011 IEEE International Conference on Robotics and Automation*, 2011, pp. 3607–3613.
- [19] C. Yuan, J. Lin, Z. Zou, X. Hong, and F. Zhang, “Std: Stable triangle descriptor for 3d place recognition,” in *2023 IEEE International Conference on Robotics and Automation (ICRA)*, 2023, pp. 1897–1903.
- [20] C. Yuan, J. Lin, Z. Liu, H. Wei, X. Hong, and F. Zhang, “Btc: A binary and triangle combined descriptor for 3-d place recognition,” *IEEE Transactions on Robotics*, vol. 40, pp. 1580–1599, 2024.
- [21] X. Xu, S. Lu, J. Wu, H. Lu, Q. Zhu, Y. Liao, R. Xiong, and Y. Wang, “Ring++: Roto-translation invariant gram for global localization on a sparse scan map,” *IEEE Transactions on Robotics*, vol. 39, no. 6, pp. 4616–4635, 2023.
- [22] X. Chen, T. Läbe, A. Milioto, T. Röhling, O. Vysotska, A. Haag, J. Behley, and C. Stachniss, “Overlapnet: Loop closing for lidar-based slam,” *arXiv preprint arXiv:2105.11344*, 2021.
- [23] Z. Liu and F. Zhang, “Balm: Bundle adjustment for lidar mapping,” *IEEE Robotics and Automation Letters*, vol. 6, no. 2, pp. 3184–3191, 2021.
- [24] Z. Liu, X. Liu, and F. Zhang, “Efficient and consistent bundle adjustment on lidar point clouds,” *IEEE Transactions on Robotics*, vol. 39, no. 6, pp. 4366–4386, 2023.
- [25] X. Liu, Z. Liu, F. Kong, and F. Zhang, “Large-scale lidar consistent mapping using hierarchical lidar bundle adjustment,” *IEEE Robotics and Automation Letters*, vol. 8, no. 3, pp. 1523–1530, 2023.
- [26] J. Li, T.-M. Nguyen, S. Yuan, and L. Xie, “Pss-ba: Lidar bundle adjustment with progressive spatial smoothing,” in *2024 IEEE/RSJ International Conference on Intelligent Robots and Systems (IROS)*, 2024, pp. 1124–1129.
- [27] S. Zhong, Y. Qi, Z. Chen, J. Wu, H. Chen, and M. Liu, “Dcl-slam: A distributed collaborative lidar slam framework for a robotic swarm,” *IEEE Sensors Journal*, vol. 24, no. 4, pp. 4786–4797, 2024.
- [28] Y. Huang, T. Shan, F. Chen, and B. Englot, “Disco-slam: Distributed scan context-enabled multi-robot lidar slam with two-stage global-local graph optimization,” *IEEE Robotics and Automation Letters*, vol. 7, no. 2, pp. 1150–1157, 2021.
- [29] H. Wei, R. Li, Y. Cai, C. Yuan, Y. Ren, Z. Zou, H. Wu, C. Zheng, S. Zhou, K. Xue, and F. Zhang, “Large-scale multi-session point-cloud map merging,” *IEEE Robotics and Automation Letters*, 2025.
- [30] P. Yin, S. Zhao, H. Lai, R. Ge, J. Zhang, H. Choset, and S. Scherer, “Automerger: A framework for map assembling and smoothing in city-scale environments,” *IEEE Transactions on Robotics*, 2023.
- [31] J. G. Mangelson, D. Dominic, R. M. Eustice, and R. Vasudevan, “Pairwise consistent measurement set maximization for robust multi-robot map merging,” in *2018 IEEE International Conference on Robotics and Automation (ICRA)*, 2018.
- [32] B. Forsgren, R. Vasudevan, M. Kaess, T. W. McLain, and J. G. Mangelson, “Group-k consistent measurement set maximization for robust outlier detection,” in *2022 IEEE/RSJ International Conference on Intelligent Robots and Systems (IROS)*, 2022.
- [33] B. Forsgren, M. Kaess, R. Vasudevan, T. W. McLain, and J. G. Mangelson, “Group-k consistent measurement set maximization via maximum clique over k-uniform hypergraphs for robust multi-robot map merging,” *The International Journal of Robotics Research*, vol. 43, no. 14, pp. 2245–2273, 2024.
- [34] N. Sünderhauf and P. Protzel, “Towards a robust back-end for pose graph slam,” in *2012 IEEE International Conference on Robotics and Automation*, 2012, pp. 1254–1261.
- [35] E. Mendes, P. Koch, and S. Lacroix, “Icp-based pose-graph slam,” in *2016 IEEE International Symposium on Safety, Security, and Rescue Robotics (SSRR)*, 2016, pp. 195–200.
- [36] T. Shan, B. Englot, D. Meyers, W. Wang, C. Ratti, and D. Rus, “Liv-sam: Tightly-coupled lidar inertial odometry via smoothing and mapping,” in *2020 IEEE/RSJ International Conference on Intelligent Robots and Systems (IROS)*, 2020, pp. 5135–5142.
- [37] T. Ma, B. Xia, Y. Ou, J. Wang, and S. Xu, “Robust second-order lidar bundle adjustment algorithm using mean squared group metric,” *IEEE Transactions on Automation Science and Engineering*, pp. 1–1, 2025.
- [38] R. Dubé, A. Cramariuc, D. Dugas, J. Nieto, R. Siegwart, and C. Cadena, “Segmap: 3d segment mapping using data-driven descriptors,” in *Robotics: Science and Systems XIV*, ser. RSS2018. Robotics: Science and Systems Foundation, Jun. 2018. [Online]. Available: <http://dx.doi.org/10.15607/RSS.2018.XIV.003>
- [39] H. Wu, Y. Li, W. Xu, F. Kong, and F. Zhang, “Moving event detection from lidar point streams,” *nature communications*, vol. 15, no. 1, p. 345, 2024.
- [40] M. A. Fischler and R. C. Bolles, “Random sample consensus: a paradigm for model fitting with applications to image analysis and automated cartography,” *Commun. ACM*, 1981.
- [41] A. Segal, D. Haehnel, and S. Thrun, “Generalized-icp,” in *Robotics: science and systems*, vol. 2, no. 4. Seattle, WA, 2009, p. 435.
- [42] R. B. Rusu, Z. C. Marton, N. Blodow, M. Dolha, and M. Beetz, “Towards 3d point cloud based object maps for household environments,” *Robotics and Autonomous Systems*, vol. 56, no. 11, pp. 927–941, 2008.

- [43] J. Li, T.-M. Nguyen, M. Cao, S. Yuan, T.-Y. Hung, and L. Xie, “Graph optimality-aware stochastic lidar bundle adjustment with progressive spatial smoothing,” *arXiv preprint arXiv:2410.14565*, 2024.
- [44] D. Feng, Y. Qi, S. Zhong, Z. Chen, Q. Chen, H. Chen, J. Wu, and J. Ma, “S3e: A multi-robot multimodal dataset for collaborative slam,” *IEEE Robotics and Automation Letters*, 2024.
- [45] Z. Chen, Y. Qi, D. Feng, X. Zhuang, H. Chen, X. Hu, J. Wu, K. Peng, and P. Lu, “Heterogeneous lidar dataset for benchmarking robust localization in diverse degenerate scenarios,” *arXiv preprint arXiv:2409.04961*, 2024.
- [46] J. Lin and F. Zhang, “R3live: A robust, real-time, rgb-colored, lidar-inertial-visual tightly-coupled state estimation and mapping package,” in *2022 International Conference on Robotics and Automation (ICRA)*, 2022, pp. 10 672–10 678.
- [47] X. Hu, J. Wu, M. Jia, H. Yan, Y. Jiang, B. Jiang, W. Zhang, W. He, and P. Tan, “Mapeval: Towards unified, robust and efficient slam map evaluation framework,” *IEEE Robotics and Automation Letters*, vol. 10, no. 5, pp. 4228–4235, 2025.